

PAPER • OPEN ACCESS

Development of a novel nanoscratch technique for quantitative measurement of ice adhesion strength

To cite this article: T Loho and M Dickinson 2018 *IOP Conf. Ser.: Mater. Sci. Eng.* **348** 012003

View the [article online](#) for updates and enhancements.

Related content

- [Evaluation of Interface Adhesion Strength in Cu/\(Ta-x% N, Ta/TaN\)/SiO₂/Si by Nanoscratch Test](#)
Atsuko Sekiguchi and Junichi Koike
- [Micro-nano Structurized Gold Chip for SPR Imaging Sensor](#)
Bing Zhang, Kai Pang, Chunfei Shi et al.
- [Analyses of Interface Adhesion between Cu and SiCN Etch Stop Layers by Nanoindentation and Nanoscratch Tests](#)
Shou-Yi Chang and Yu-Shuien Lee

Development of a novel nanoscratch technique for quantitative measurement of ice adhesion strength

T Loho¹ and M Dickinson²

1 PhD Student, Department of Chemical and Materials Engineering, University of Auckland, Auckland, NZ

2 Senior Lecturer, Department of Chemical and Materials Engineering, University of Auckland, Auckland, NZ

E-mail: tloh003@aucklanduni.ac.nz

Abstract. The mechanism for the way that ice adheres to surfaces is still not well understood. Currently there is no standard method to quantitatively measure how ice adheres to surfaces which makes ice surface studies difficult to compare. A novel quantitative lateral force adhesion measurement at the micro-nano scale for ice was created which shears micro-nano sized ice droplets (less than 3 μm in diameter and 100nm in height) using a nanoindenter. By using small ice droplets, the variables associated with bulk ice measurements were minimised which increased data repeatability compared to bulk testing. The technique provided post-testing surface scans to confirm that the ice had been removed and that measurements were of ice adhesion strength. Results show that the ice adhesion strength of a material is greatly affected by the nano-scale surface roughness of the material with rougher surfaces having higher ice adhesion strength.

1. Introduction

Ice formation and adhesion can lead to various hazards and economical losses in modern society. For example, the presence of ice under aircraft wings or boat hulls increase the vehicles weight and drag coefficient [1], impairing their performance. In areas with extreme winters, accretion of ice can lead to downed power lines and road blocks [2]. One solution to this problem is to remove the ice using mechanical or thermal methods (active de-icing), but this is energy intensive [3]. Recent literature has instead focussed on passive de-icing methods which create a surface that prevents ice from building up on the surface. This can be done by minimising the formation of condensation of water on the surface or improving the roll-off behaviour of the condensed droplets which prevent frost formation [4-6]. Other researchers have tried to prevent ice formation by reducing the mechanical adhesion shear stress of the ice-substrate interface. This includes various coatings [6,7], textured surfaces [8], or infusing porous surfaces with liquid lubricants [9].

The effectiveness of these methods is usually characterised by measuring the ice adhesion strength, defined as the shear stress required to remove ice from the surface. Various methods were developed to measure ice adhesion strength at the macro-scale, for example by mechanically shearing solid ice structures [10], using torsion to shear ice layer from a pillar [11], or using centrifugal force [12]. These methods produce different results from one another for the same surface because there are numerous variables that affect the results such as the shape and size of ice, loading rate, time of contact, sample cooling rate, sample size, and many more [11]. Table 1 shows the values of ice adhesion strength of polished stainless steel measured with different testing methods done by various researchers.



Table 1. Values of ice adhesion strength measured with different testing methods for stainless steel

Literature	Year	Surface Temperature (°C)	Ice Adhesion Strength (kPa)
Raraty, L et al [13]	1958	-10	1590 to 1960
Jellinek, H [14]	1959	-4.5	67 ± 24
Petrenko, V et al [15]	1999	-10	14 to 70
Chen, J et al [16]	2014	-15	647 ± 125
Ling, E et al [17]	2016	-15	682 ± 46
Matsumoto, K et al [18]	2016	-5	3240

Micro-nano scale ice adhesion strength testing can give more objective results of ice adhesion strength and reduce some of the variables which affect macro-scale ice adhesion strength. Matsumoto *et al* demonstrated this by measuring the true ice adhesion strength of various materials in the nano-scale using Scanning Probe Microscopy (SPM) technique and found that the ice adhesion strength of a surface is higher than what was previously measured in the macro-scale [18-20].

In this study, a new way to measure ice adhesion strength using a nanoscratch technique was investigated. This is based on a technique developed by Dickinson *et al* to measure true adhesion strength of microscopic ceramic cold-spray splats [21]. By controlling the temperature of the sample during nanoindentation test, micro-nano sized water droplets can be condensed on the surface that will then freeze into micro-nano sized ice droplets. Using nano-scratch technique as the basis, the ice droplets can be sheared off the surface and ice adhesion strength can be measured.

Stainless steel was selected as a sample due to its common use in commercial and engineering applications [22]. Xenon was used as the inert gas ion source due to its high atomic mass (131.29 g.mol⁻¹) which leads to a higher sputtering yield than lighter noble gases. Studies have shown that nano-scale ripple patterns arise during ion implantation and the formation is dependent on the angle of incidence of the ion beam as well as the crystallographic orientation of the grains [23, 24]. In metals, the ripples have been found to vary between different grains on the surface, which has been attributed to preferential sputtering of metal grains with different crystallographic orientations on the surface [25], impurities, and surface atom diffusion [26, 27].

2. Experimental procedure

2.1. Stainless steel samples

Grade 316 stainless steel with a BA (Bright Annealed) surface finish was cut into six 10 × 12 mm pieces and then cleaned with acetone wipes. The samples were 1 mm thick. The BA surface finish is the industry standard for a smooth, bright, reflective stainless steel surface according to the Standard Specification for General Requirements for Flat-Rolled Stainless and Heat-Resisting Steel Plate, Sheet, and Strip ASTM A480/A480M standard.

Five of the samples were ion implanted with Xe⁺ ions to induce atomic sputtering and create sub-micron features on the surface of the stainless steel. Xe⁺ ions were extracted from a Penning ion source at an accelerating voltage of 20 kV and selected with a 90 ° mass analyser magnet [28]. To limit a significant increase in the temperature of the samples, the ion beam current density for all ion implantation experiment was kept within 7 to 10 μA.cm⁻². These ions were then implanted into the surface with different fluences ranging from 10¹⁶ to 10¹⁸ ions.cm⁻² at 0 ° and 45 ° angle of incidence to promote nano-scale features formation. During ion implantation, the pressure of the chamber was at 7 × 10⁻⁵ Pa. Table 2 shows the different ion implantation conditions applied to the sample. Simulation of the ion implantation using the Dynamic Transport of Ion in Matter (D-TRIM) software [29] yielded sputtering depths shown in Table 2.

Table 2. Different ion beam treatment conditions on the stainless steel substrate. The sputtered depths were calculated using the D-TRIM software.

#	Sample Name	Fluence (ions.cm ⁻²)	Incident Angle of Ions	Sputtered Depth (nm)
1	Control	n/a	n/a	n/a
2	1E16Xe0	1×10^{16}	0°	8.56
3	5E16Xe0	5×10^{16}	0°	39.3
4	1E17Xe0	1×10^{17}	0°	86.8
5	1E17Xe45	1×10^{17}	45°	162
6	1E18Xe45	1×10^{18}	45°	1670

2.2. Topography measurement

The samples were cleaned using an ultrasonic acetone bath for 5 minutes prior to characterisation. The surface roughness of the samples was characterised using a Bruker Contour GT-K Optical Profiler to measure Root Mean Square (RMS) roughness (R_q) values. With a $5\times$ objective magnification lens and operating under the VSI mode, the optical profiler provided a vertical resolution of 3 nm and a lateral resolution of 2 μm . Vision64 software (Bruker) was used to analyse the data and generate 3D profile images. Five $960 \times 720 \mu\text{m}$ rectangular measurements at random spots on the surface of each sample were taken and averaged. SEM images were captured using an FEI Quanta 200F Scanning Electron Microscope. Secondary electrons were detected by an Everhart-Thornley Detector.

2.3. Micro-nano scale ice adhesion strength testing

Nanoscratch testing was carried out using the Hysitron TI-950 Triboindenter machine with a 3 μm fluid cell diamond cono-spherical tip (Hysitron). A fluid cell tip was used because of its extended shaft made from a ceramic-based material (Macor) that prevents thermal conduction from the piezoelectric transducer of the nanoindenter that could melt the ice droplets during testing. Humidity of the testing chamber was controlled by flowing dry N_2 gas into the testing chamber until the relative humidity was measured to be 15%.

Surface temperature was controlled using a custom-made thermoelectric cooling device with a mild steel base plate on the cold side and a water-cooled heat sink on the hot side. The schematic of this device is shown in Figure 1. The cooling stage is based on a 195 W thermoelectric Peltier cooler module (APH-199-17-10-E, European Thermodynamics). An aluminium heat sink with a heat transfer area of $2.6 \times 10^{-3} \text{ m}^2$ was constructed to remove heat from the hot side of the module. The heat sink is connected to a peristaltic pump that circulates 3 $\text{mL}\cdot\text{s}^{-1}$ of cold water (approximately 15 °C) inside it. The plastic casing and screws were 3D-printed ABS polymer designed to prevent heat loss to the surrounding environment and compress all the components together, removing any air bubbles between them.

Temperature reading is obtained from a thermistor (MP-3193, TE Technology Inc.) that reads the temperature of the mild steel base plate. To control the temperature, the Peltier module and the thermistor is connected to a Pulse Width Modulation (PWM) temperature controller (TC-48-20, TE Technology Inc.) that controls the voltage applied to the module based on the temperature reading from the thermistor. To promote thermal conduction between the heat sink, the Peltier module, the thermistor and the mild steel base plate; a layer of high-density polysynthetic silver thermal compound (Arctic Silver 5, Arctic) was applied between them. The whole stage was then placed in a safety wall made from mild steel to prevent spilling of water to the nanoindenter stage in case of leakage. The sample was fixed on the mild steel base plate using a small amount of cyanoacrylate adhesive.

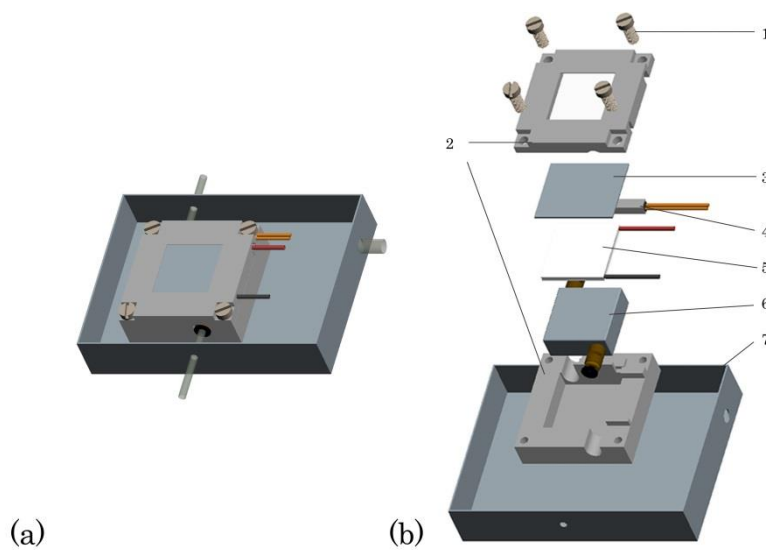


Figure 1. Custom made thermoelectric cooling device for sub-zero temperature nanoscratch testing. (a) Assembled view. (b) Exploded view of the components: (1) Plastic screws (2) Insulating plastic casing (3) Mild steel base plate (4) Thermistor (5) 195 W Thermoelectric Peltier module (6) Water cooled aluminium heat sink (7) Safety walls to prevent spillage of water in case of leakage.

The micro-nano scale ice adhesion strength testing started with performing indents on the surface to serve as a landmark, and then performing a Scanning Probe Microscopy (SPM) scan on the area by rastering a $20 \times 20 \mu\text{m}$ surface of the sample at room temperature with the nanoindenter tip set at a $2 \mu\text{N}$ force setpoint. From this point onward, this image is referred to as the 'Pre-Test' SPM scan.

After the pre-test SPM scan was obtained, the nanoindenter tip was raised 100 nm above the surface and the cooling stage was turned on to reduce the surface temperature to -5°C . This process took approximately 2 minutes before the temperature was stable, as shown in Figure 2. During this time, water droplets condensed from the surrounding air and subsequently froze into ice droplets. Due to the high thermal conductivity of the diamond tip, this process also significantly cooled the diamond cono-spherical tip of the nanoindenter and prevent melting of the ice droplets during nanoscratch testing.

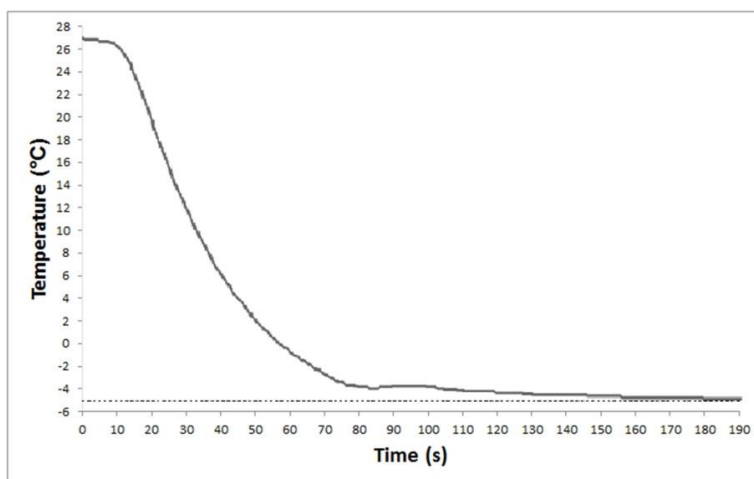


Figure 2. Temperature of the mild steel base plate over time as the cooling stage is turned on. During testing, the temperature remained stable at $-5 \pm 0.5^\circ\text{C}$ for at least two continuous hours.

After more than two minutes had passed and the surface temperature had stabilised at -5°C , the tip was lowered into contact with the sample. Another $20 \times 20 \mu\text{m}$ SPM scan of the surface was done with the nanoindenter tip set at $2 \mu\text{N}$ force setpoint at -5°C . This image is called the 'Pre-Scratch' SPM scan image. New features that were found in the Pre-Scratch image that were not in the Pre-Test image were assumed to be ice droplets that formed on the surface of the sample. A sample comparison between the Pre-Test and Pre-Scratch image of the polished stainless steel substrate is shown in Figure 3. The diameter of the ice droplet was measured using the Hysitron TriboView software to analyse the

Pre-Scratch image. Testing was done on ice droplets that are smaller than $3\ \mu\text{m}$ in diameter (less than the tip's radius of curvature) to ensure the nanoscratch tip sheared the whole ice droplet and not cut through it. Once a suitable ice droplet had been found, the tip was centred above that particular ice droplet.

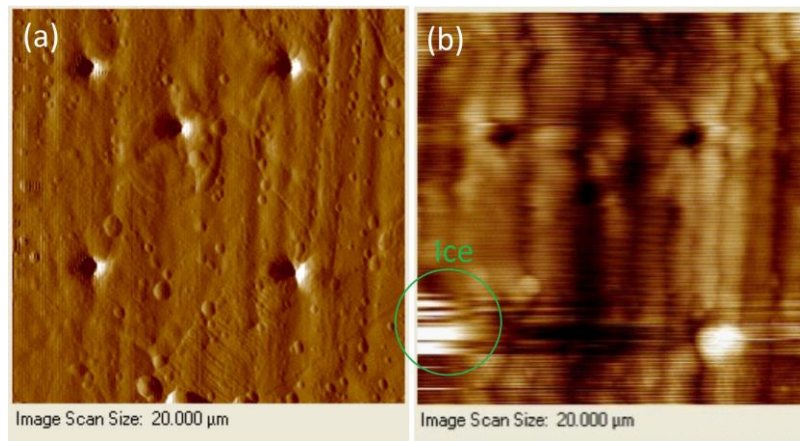


Figure 3. Gradient Forward (GF) images of the (a) Pre-Test SPM scan at room temperature and (b) Pre-Scratch SPM scan at -5°C of the polished stainless steel sample. Note that the blurriness of the Pre-Scratch image at (b) is due to the slight vibration caused by cooling water running in the heat sink. The circle on the Pre-Scratch image indicates the ice droplet that formed during the test. The tip had sliding effects at lines where the ice was found due to the slipperiness of ice droplets.

The nanoscratch test began with the tip moving $5\ \mu\text{m}$ vertically to measure the tilt of the sample. The testing procedure consists of three steps, shown in the load function in Figure 4.

1. **Pre-Scan** scans the surface of the sample as the nanoindenter tip is moved $10\ \mu\text{m}$ vertically with $0\ \mu\text{N}$ axial force. The purpose of this step is to ensure that the ice droplet to be scratched is on the path of the nanoscratch test.
2. **Scratch** moved the tip $10\ \mu\text{m}$ vertically in the other direction with $150\ \mu\text{N}$ axial force to apply shear stress and remove the ice from the surface. $150\ \mu\text{N}$ is selected as the axial force through trial and error as the amount of force large enough to remove the ice from the surface but not large enough to make the tip dig through the steel surface.
3. **Post-Scan** scans the surface of the sample $10\ \mu\text{m}$ vertically after the nanoscratch was done to confirm removal of the ice droplet.

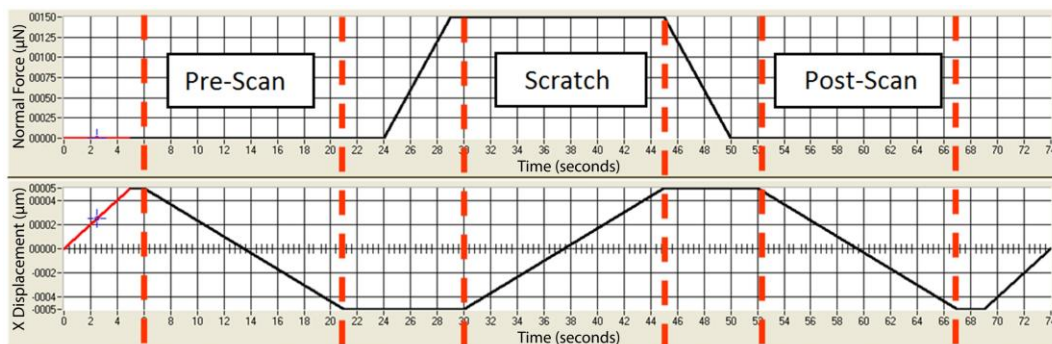


Figure 4. The load function of the nanoscratch testing procedure. The top graph shows the normal force actuated on the tip over time, while the bottom graph shows the lateral displacement of the tip over time. The load function was divided into three steps during the ice adhesion strength measurement.

3. Results and discussion

3.1. Sample topography

Optical profilometry revealed that for the first four fluences, the ion implantation process slightly increases the surface roughness of the steel. The ion implantation process creates roughness features on the surface of the steel through atomic sputtering from the xenon ions. On the 1E18Xe45 sample, it can be seen that the roughness increased significantly and a much rougher surface was created. The RMS roughness values and the 3D surface plot of the samples are shown in Figure 5.

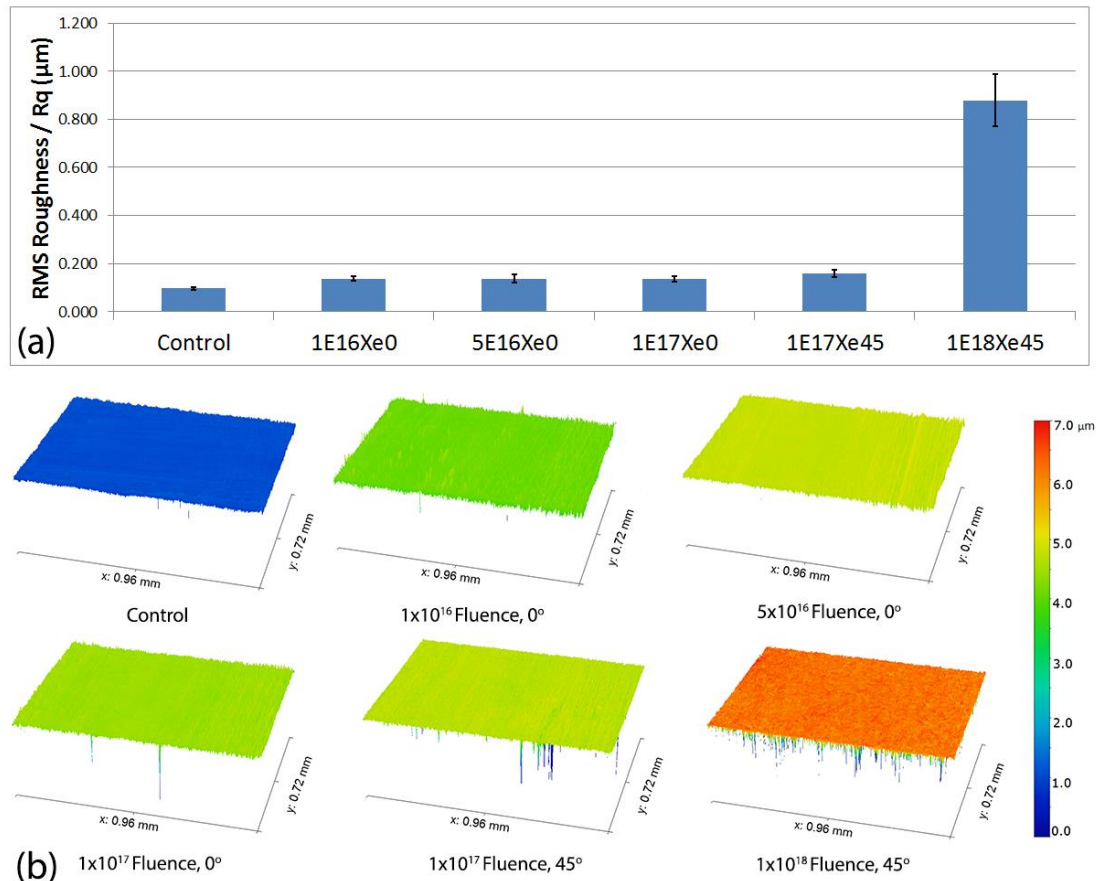


Figure 5. (a) RMS roughness and (b) 3D surface plot of the polished and ion implanted stainless steels with different fluences obtained from the optical profiler. Error bars show one standard deviation from five repeat measurements.

In order to confirm the presence of sub-micron scale features on the surface of the stainless steel, SEM images were taken at random spots on the surface of the samples, shown in Figure 6. Other than the 1E18Xe45 sample, the surfaces were seen to be relatively smooth with shallow roughness features. In the 1E18Xe45 sample, it can be seen that there are ripple patterns within the grain of the ion implanted samples, contributing to the increased roughness values measured by the optical profiler.

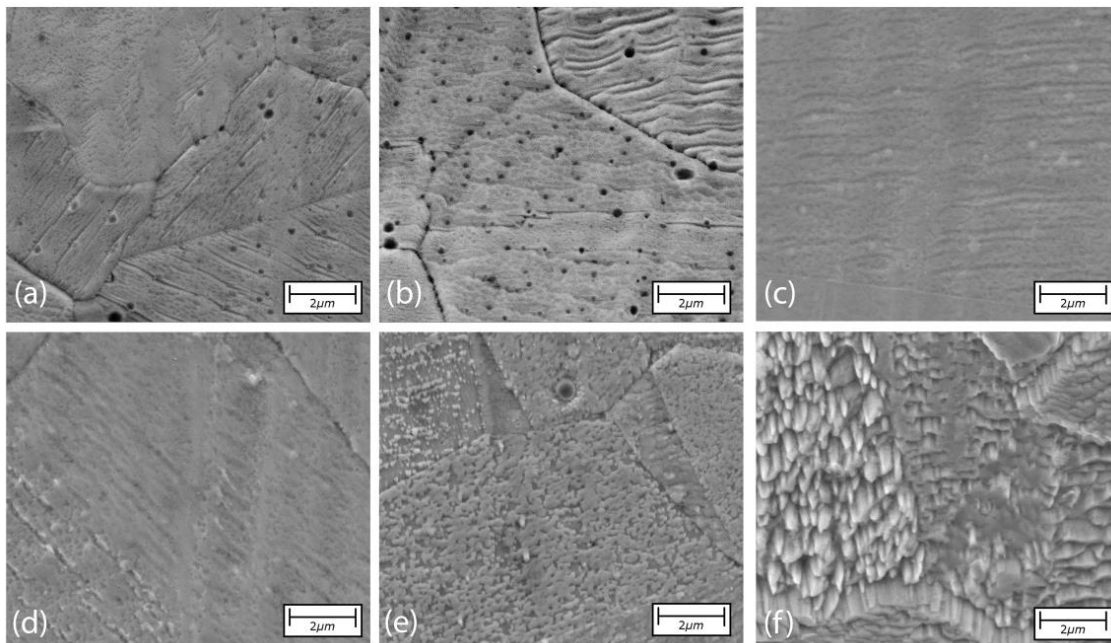


Figure 6. Secondary electrons SEM images of the (a) Control sample, (b) 1E16Xe0 sample, (c) 5E16Xe0 sample, (d) 1E17Xe0 sample, (e) 1E17Xe45 sample, and (f) 1E18Xe45 sample.

3.2. Nanoscratch result analysis

To prevent overestimation of the ice droplet's diameter from the SPM scan due to the slipperiness of ice, the vertical distance of an ice droplet is measured from the Pre-Scratch SPM scan image with the Hysitron TriboView software. This is shown for the polished steel in Figure 7a and 7b and the effect is illustrated in Figure 7c. As can be seen from Figure 7b, if the horizontal distance was taken, the diameter of the ice can be overestimated by more than double the actual diameter of the ice. In this example, the ice droplet scratched was $0.74 \mu\text{m}$ in diameter and 74 nm in height. Since the ice droplet was relatively small, it can be assumed that the condensed droplet had a circular area of contact with the surface.

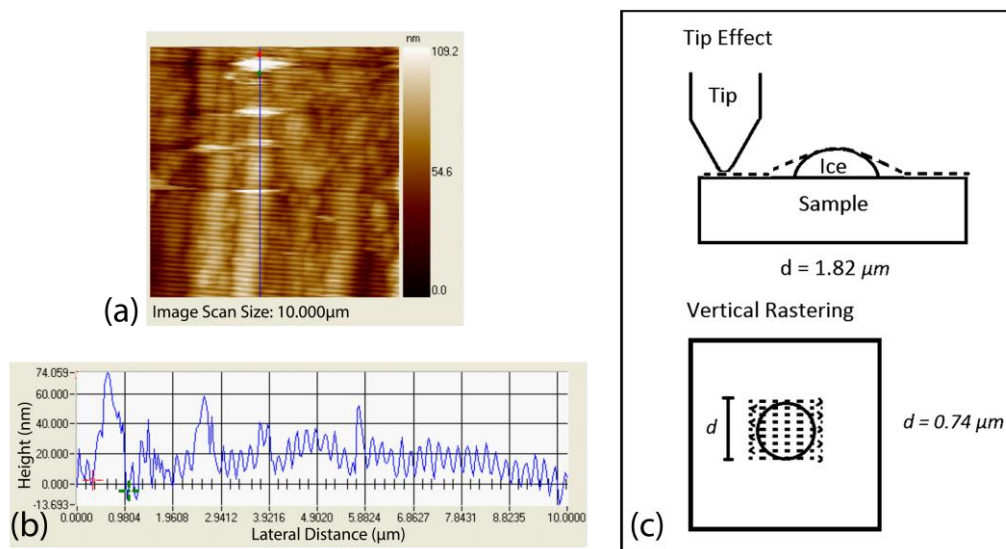


Figure 7. Determination process of an ice droplet diameter. (a) Pre-Scratch SPM image of an ice droplet; (b) Line topography profile of the SPM image shown in (a); and (c) Schematic showing why vertical distance was taken as the diameter of the ice droplet instead of the horizontal distance.

Once the size of the ice droplet was determined, a nanoscratch test according to the load function shown in Figure 4 was performed. A sample scratch result for the ice droplet measured in Figure 7a is shown in Figure 8. The analysis started by looking at the top right graph of normal displacement over time during the 'Pre-Scan' step ($t = 5$ to 21 s). The presence of ice was confirmed by the 'bump' (approximately 75 nm in height, similar to the ice droplet measured in Figure 7a) detected by the tip. The next step was to find the position of this bump during the 'Scratch' step of the load function. This was done by drawing a horizontal line from the position of the ice droplet at the bottom right graph of lateral displacement over time. At this position, it can be seen in the bottom left graph of lateral force over time that the tip measured a jump in force when the ice was scratched. In this example, the lateral force was measured to be 11.1 μN and this value was taken as the ice adhesion force of the sample.

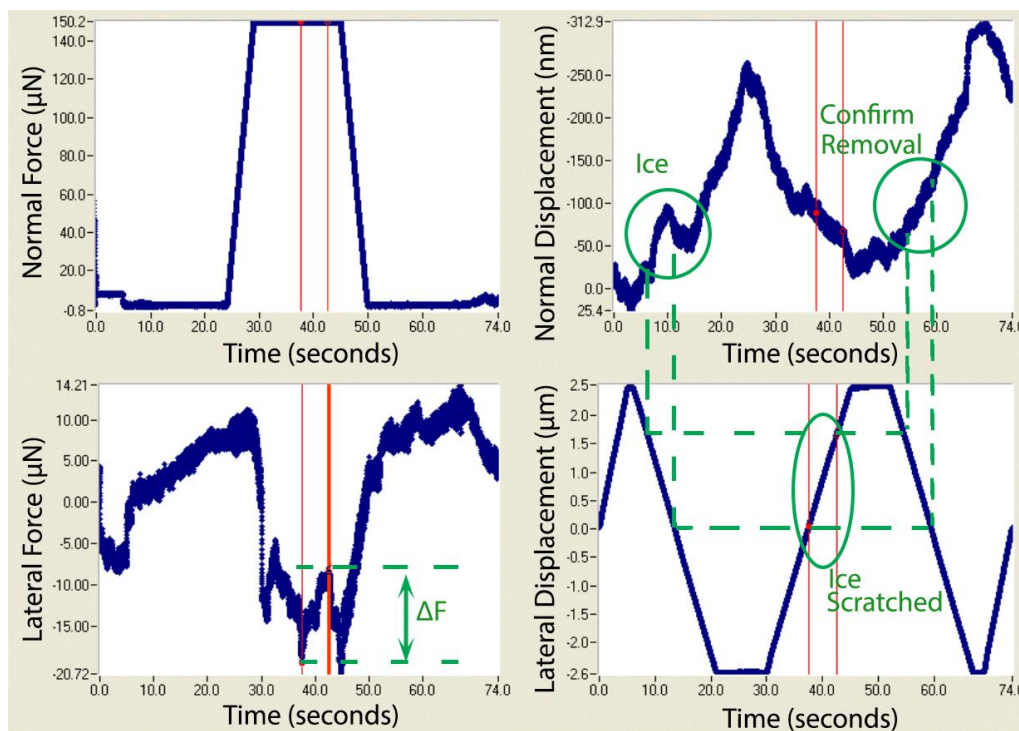


Figure 8. Scratch data obtained from the Hysitron TriboScan software during ice adhesion strength measurement after tilt correction. The four graphs shown are (top left) normal force over time (top right) normal displacement over time (bottom left) lateral force over time and (bottom right) lateral displacement over time.

The last step was to interpolate the position of the scratched ice to the 'Post-Scan' step of the load function to confirm full removal of the ice droplet from the surface, affirming that full adhesive failure had occurred. Not all of the tests resulted in full adhesive removal of the ice droplet and sometimes the Post-Scan step revealed that there was ice left behind after the scratch. These results were not considered in this study as the failure involved both adhesion and cohesion.

The ice adhesion strength of the sample was then calculated by dividing the ice adhesion force with the area of the ice droplet measured previously. In this particular example the ice adhesion strength of the polished steel was calculated to be 4.3 MPa, which is in the same order of magnitude as the nano-scale ice adhesion strength of stainless steel measured by Matsumoto *et al* [18].

3.3. Ice adhesion strength of stainless steel samples

The experiment was repeated on ten different areas of the steel samples and the results shown in Figure 9. It can be seen that the ice adhesion strength of the first five samples were not significantly

different at all. This is likely because the first five samples had very similar roughness measurement and similar surface topography.

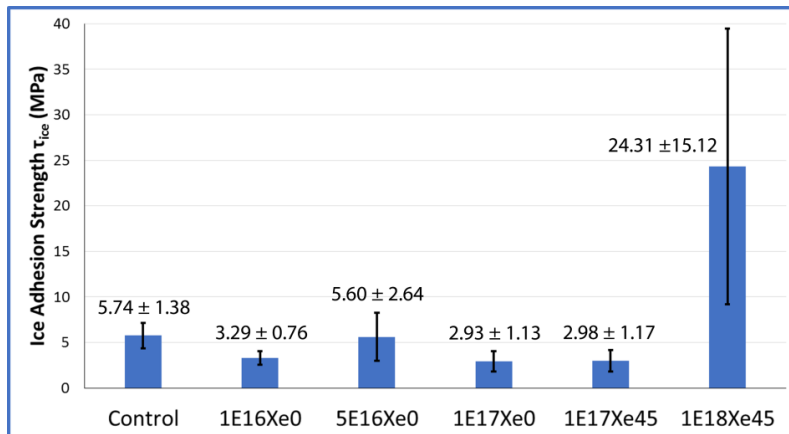


Figure 9. Mean ice adhesion strength of the polished and ion implanted stainless steels from ten repeat measurements. Error bars show one standard deviation.

Comparing this result with the ice adhesion strength values measured by different researchers in Table 1, it can be seen that this novel method yielded results in the same order of magnitude as the works of Matsumoto *et al* [18] for ice adhesion strength measurement in the nano-scale. As previously mentioned in Section 1, the true ice adhesion strength measured in the micro-nano scale was reported to be higher than the ice adhesion strength measured in the macro scale. This is thought to be caused by the absence of variables within the ice itself (e.g. impurities and air bubbles within the ice) when the size of the ice is very small. Since those variables promoted cohesive failure within the ice and could also induce pre-existing cracks, the ice adhesion strength measured in the micro-nano scale is much more dependent on the properties of the surface, such as its surface energy and topography, rather than the properties of the ice. The measured values are hence closer to the true ice adhesion strength of the surface.

It can be seen that the ice adhesion strength of the much rougher 1E18Xe45 ion implanted steel was significantly higher than the ice adhesion strength of the smoother polished steel sample and the other ion implanted samples where the roughness was not significantly modified. This is likely caused by the fact that a rougher surface had a much higher true contact area than a smooth surface for the same apparent contact area. This effect is illustrated in Figure 10. This is especially true in the case of ice because as the water droplet freezes, it expanded into the asperities, removing any air bubbles that might have been trapped between the surface of the water droplet and the solid. Because of the much higher true contact area, there was increased interaction between the solid surface and the ice droplet.

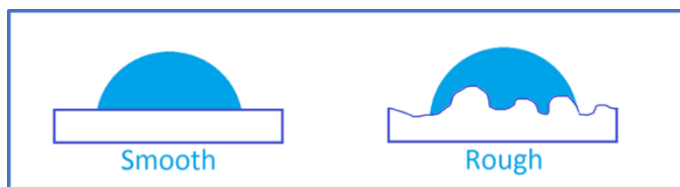


Figure 10. Schematic showing how a rough surface would have more true contact area than a smooth surface for the same apparent contact area.

4. Conclusions

A novel way to measure ice adhesion strength of materials in the micro-nano scale was developed in this study to enable a more objective and repeatable data unaffected by various factors that influence macro-scale ice adhesion failures. Moreover, by performing a post-scan of the surface after the nanoscratch procedure, the complete removal of the ice could be confirmed to ensure failure through adhesion and not cohesion which can occur in macro-scale ice adhesion tests. By performing the test on surfaces with different roughness values, it can be seen that the true ice adhesion strength is much

higher for a rougher surface than a smoother surface, as a rougher surface would have much higher true contact area for the same apparent contact area.

With the development of this micro-nano scale ice adhesion strength testing method, objective comparison between ice adhesion strength reduction studies can be made easier. The advantages of this technique include the microscopic size of ice droplets, the force resolution of the nanoscratch technique that can measure μN forces, the ability to do post-scans of the surface to confirm full removal of the ice, and the stability of the substrate temperature achieved by the water-cooled thermoelectric cooler. All of this leads to a more objective result of ice adhesion strength measurement that are easy and repeatable.

5. References

- [1] Civil Aviation Authority of New Zealand 2000 *Aircraft Icing Handbook* (Civil Aviation Authority (CAA))
- [2] Laforte J, Allaire M and Laflamme J 1998 *Atmospheric Research* **46** 143–158
- [3] Frankenstein S and Tuthill A M 2002 *Journal of Cold Regions Engineering* **16** 83–96
- [4] Mishchenko L, Hatton B, Bahadur V, Taylor J A, Krupenkin T and Aizenberg J 2010 *ACS Nano* **4** 7699–7707
- [5] Boinovich L B, Emelyanenko A M, Ivanov V K and Pashinin A S 2013 *ACS Applied Materials and Interfaces* **5** 2549–2554
- [6] Golovin K, Kobaku S P R, Lee D H, DiLoreto E T, Mabry J M and Tuteja A 2016 *Science Advances* **2**
- [7] Menini R and Farzaneh M 2011 *Journal of Adhesion Science & Technology* **25** 971–992
- [8] He Y, Jiang C, Cao X, Chen J, Tian W and Yuan W 2014 *Applied Surface Science* **305** 589–595
- [9] Kim P, Wong T S S, Alvarenga J, Kreder M J, Adorno-Martinez W E and Aizenberg J 2012 *ACS Nano* **6** 6569–6577
- [10] Bascom W D, Cottington R L and Singleterry C R 1969 *The Journal of Adhesion* **1** 246–263
- [11] Makkonen L 2012 *Journal of Adhesion Science and Technology* **26** 413–445
- [12] Laforte C and Beisswenger A 2005 *International Workshop on Atmospheric Icing of Structures XI*
- [13] Raraty L E and Tabor D 1958 *Proceedings of the Royal Society of London. Series A, Mathematical and Physical Sciences* **245** 184–201
- [14] Jellinek H 1959 *Journal of colloid science* **14** 268–280
- [15] Petrenko V F 1999 *Physics of ice* (Oxford: Oxford)
- [16] Chen J, Luo Z, Fan Q, Lv J and Wang J 2014 *Small (Weinheim an der Bergstrasse, Germany)* **10** 4693–9
- [17] Ling E J Y, Uong V, Renault-Crispo J S, Kietzig A M and Servio P 2016 *ACS Applied Materials and Interfaces* **8** 8789–8800
- [18] Matsumoto K, Honda M, Minamiya K, Tsubaki D, Furudate Y and Murase M 2016 *International Journal of Refrigeration* **66** 84–92
- [19] Matsumoto K and Daikoku Y 2009 *International Journal of Refrigeration* **32** 444–453
- [20] Matsumoto K, Akaishi M, Teraoka Y, Inaba H and Koshizuka M 2012 *International Journal of Refrigeration* **35** 130–141
- [21] Dickinson M E and Yamada M 2010 *Nanoscience and Nanotechnology Letters* **2** 348–351
- [22] Cobb H M 2010 *The History of Stainless Steel* (ASM International) pp 193–228
- [23] Bradley R M and Harper J M E 1988 *Journal of Vacuum Science & Technology A: Vacuum, Surfaces, and Films* **6** 2390–2395
- [24] Valbusa U, Boragno C and Mongeot F B D 2002 *Journal of Physics: Condensed Matter* **14** 8153–8175
- [25] Odnobokova M, Kipelova a, Belyakov a and Kaibyshev R 2014 *IOP Conference Series: Materials Science and Engineering* **63** 012060
- [26] Ochoa E A, Droppa R, Basso R L O, Morales M, Cucatti S, Zagonel L F, Czerwicz T, Dos Santos M C, Figueroa C A and Alvarez F 2013 *Materials Chemistry and Physics* **143** 116–123
- [27] Cucatti S, Ochoa E A, Morales M, Jr R D, Garcia J, Pinto H C and Zagonel L F 2015 4140

[28] Markwitz A and Kennedy J 2009 *International Journal of Nanotechnology* **6** 369–383

[29] Chakarov I R, Todorov S S and Karpuzov D S 1992 *The Journal of Physical Chemistry C* **69** 193–199

Acknowledgements

This work is funded by the University of Auckland Doctoral Scholarship programme with the help of Dr. Jerome Leveneur and Dr. John Kennedy from National Isotope Centre, Lower Hutt, New Zealand.